Nanoscale mapping of non-uniform heterogeneous nucleation kinetics mediated by surface chemistry

Mei Wang,[1] Thilini U. Dissanayake,[1] Chiwoo Park,[2] Karen Gaskell,[3] Taylor J. Woehl[1,*]

[1]Department of Chemical and Biomolecular Engineering, University of Maryland, College Park, Maryland 20742, United States

[2]Department of Industrial and Manufacturing Engineering, Florida State University, Tallahassee, Florida 32306, United States

[3]Department of Chemistry & Biochemistry, University of Maryland, College Park, Maryland 20742, United States

[*]Corresponding author, email: tjwoehl@umd.edu

Abstract

Nucleation underlies the formation of many liquid-phase synthetic and natural materials with applications in materials chemistry, geochemistry, biophysics, and structural biology. Most liquid-phase nucleation processes are heterogeneous, occurring at specific nucleation sites at a solid-liquid interface; however, the chemical and topographical identity of these nucleation sites and how nucleation kinetics vary from site-to-site remains mysterious. Here we utilize *in situ* liquid cell electron microscopy to unveil counterintuitive nanoscale non-uniformities in heterogeneous nucleation kinetics on a macroscopically uniform solid-liquid interface. Time-resolved *in situ* electron microscopy imaging of silver nanoparticle nucleation at a water-silicon nitride interface showed apparently randomly-located nucleation events at the interface. However, nanometric maps of local nucleation kinetics uncovered nanoscale interfacial domains with either slow or rapid nucleation. Interestingly, the interfacial domains vanished at high supersaturation ratio, giving way to rapid spatially uniform nucleation kinetics. Atomic force microscopy and nanoparticle labeling experiments revealed a topographically flat, chemically heterogeneous interface with nanoscale interfacial domains of functional groups similar in size to those observed in the nanometric nucleation maps. These results, along with a semi-quantitative nucleation model, indicate that a

chemically non-uniform interface presenting different free energy barriers to heterogeneous nucleation underlies our observations of non-uniform nucleation kinetics. Overall, our results introduce a new imaging modality, nanometric nucleation mapping, and provide important new insights into the impact of surface chemistry on microscopic spatial variations in heterogeneous nucleation kinetics that have not been previously observed.

Introduction

Nucleation is the first step in a liquid to solid phase transition and as such is an important and ubiquitous process in natural and synthetic chemical and physical processes. Nucleation mediates diverse processes, such as ice and cloud formation in the atmosphere,[1] polymorph control during crystallization of pharmaceuticals,[2] chemical synthesis of nanocrystals,[3] and biomineralization.[4, 5] Despite its universal occurrence and critical role in influencing properties of a crystallizing solid phase, nucleation remains poorly understood.

Most nucleation processes are heterogeneous, occurring at an interface that lowers the free energy barrier for nucleation.[6] The topology and chemistry of the interface both mediate the heterogeneous nucleation kinetics. For example, porous materials have been used to concentrate protein molecules to form nuclei, where the pore geometry and size greatly influence nucleation rate.[6-8] Surface chemistry has also been demonstrated to impact heterogenous nucleation kinetics, where functional groups can serve as nucleation sites.[6, 9, 10] For instance, binding of precursor ions to certain functional groups has been shown to increase nucleation rate of calcium carbonate by increasing the local supersaturation ratio[10] or decreasing the overall interfacial energy of the nuclei.[11] However, it remains challenging to identify precisely how the nature of heterogeneous nucleation sites impacts nucleation kinetics, due to the lack of experimental characterization methods capable of identifying discrete nucleation events at the salient time and spatial scales.

Nucleation is difficult to probe because nuclei are sub-nanometer in size and appear stochastically and transiently in time.[12] Current experimental approaches are limited in visualizing where and when nucleation occurs. Nucleation kinetics can be inferred from optical microscopy,[9] but one must assume constant growth rate over the time it takes the nuclei to reach observable size. *In situ* atomic force microscopy (AFM) has long been utilized to observe nucleation at solid-liquid interfaces, primarily for protein and molecular crystallization.[13-18] However, the resolution of AFM is still low (~10 nm) compared to the expected sub-nanometer size of inorganic nuclei and has poor time resolution except in all but the newest generation of fast AFMs, limiting its ability to isolate nucleation in time and space. Liquid cell transmission electron microscopy (LC-TEM) is an emerging and promising approach for visualizing nucleation due to its high temporal and spatial resolution. Most research utilizing LC-TEM has focused on growth[19-22] or etching dynamics[23-25] of nanoparticles with only a few studies using LC-TEM to observe nucleation.[26-28] Further, understanding of the electron beam induced changes to solution chemistry during LC-TEM imaging is still in nascent stages,[27, 29-33] making control over important nucleation parameters like supersaturation ratio difficult.

In this article, we utilize liquid cell scanning transmission electron microscopy (LC-STEM) to spatially map heterogeneous nucleation kinetics of silver nanocrystals at a solid/liquid interface. In a previous article,[27] we established a controllable and reproducible solution chemistry for LC-STEM and determined that ensemble nucleation rate of silver nanocrystals was proportional only to LC-STEM imaging magnification, opening the door to utilize this imaging parameter as a surrogate for supersaturation ratio. Here, by correlating the nucleation kinetics of individual nanoparticles with their spatial position at the interface, we have discovered silver nanoparticle nucleation on a macroscopically uniform silicon nitride-water interface proceeds *via* preferential

heterogeneous nucleation on nanoscale interfacial domains of functional groups. Chemical force microscopy (CFM) and nanoparticle labeling experiments revealed hydrophilic domains of functional groups on the interface with similar size as the domains observed in the nucleation maps. This mechanism is further supported by a phenomenological nucleation model based on classical nucleation theory (CNT). More broadly, our results directly show that microscopic variations in surface chemistry on a macroscopically homogeneous surface can lead to microscopic variations in heterogeneous nucleation kinetics.[9, 34, 35] This new insight has broad implications for processes where heterogeneous nucleation is important, including biomineralization,[4, 5, 36, 37] nanomaterial synthesis (*e.g.* seeded nanoparticle synthesis, supported catalyst synthesis),[38-41] and hybrid inorganic-organic material synthesis (*e.g.* MOFS, halide perovskites).[42-50]

Results and Discussion

The nucleation of silver nanocrystals was visualized in real-time by low magnification LC-STEM imaging (**Figure 1a-d**). Here the electron beam reduces silver ions into silver atoms, which become supersaturated in solution causing nucleation and growth.[29] To avoid oxidative etching of nuclei, experiments were carried out in a strong reducing environment created by aqueous electrons and hydrogen radicals, with 0.1 M tert-butanol added to scavenge oxidizing species.[27] Quantitative analysis of the LC-STEM movies showed the number of silver nanocrystals increased over several minutes with an overall rate that increased with the image magnification (**Figure 1e**). We note that we do not directly visualize nuclei but instead detect them indirectly once they reach a size of ~4 nm in diameter. Nanocrystals were immobile throughout the nucleation and growth process, suggesting they formed by heterogeneous nucleation at the solid-liquid interface between the silicon nitride membrane and liquid. A single nucleation rate was not observed for each

condition (cf. **Figure 1e**), so instead we quantified the nucleation induction time (t_{ind}) of each nanocrystal, which is defined as the time between the start of LC-STEM imaging and the time required for a particle to grow to a detectible size.[28] Nucleation induction time is inversely proportional to nucleation rate and is a common metric for quantifying nucleation kinetics when there is insufficient spatial/temporal resolution to directly identify nuclei.[12] **Figure 1f** shows the nucleation induction time distribution for three different LC-STEM magnifications. The distribution shifts to shorter induction times with increasing magnification, indicating more rapid formation of nuclei. The median nucleation induction time decreased nearly linearly with increasing LC-STEM magnification and was inversely proportional to the initial silver ion concentration (**Figure 1g**). Taken together, these results indicate the nucleation rate was proportional to both image magnification and precursor concentration, suggesting these two parameters are directly proportional to the supersaturation ratio. While we cannot directly determine the supersaturation ratio of silver atoms in these experiments, it is approximated to be on the order of $S = \frac{C_{Ag}}{C_{Ag,0}} = 10^7$ (see Supporting information methods for derivation). This value is similar to a previous LC-TEM study on multi-step nanoparticle nucleation[26] and estimates for flask-based nanocrystal synthesis.[51]

For a given supersaturation ratio, some nanocrystals clearly nucleate more rapidly than others, but a cursory look at the time lapsed LC-STEM images in **Figure 1a-d** would make it seem that nucleation occurs at random spatial locations on the solid/liquid interface. This idea is further supported by the seemingly flat, homogeneous interface created between the microfabricated silicon nitride and liquid. However, a more detailed look revealed spatially varying nucleation kinetics across the interface. **Figure 2** shows nucleation flux maps, where the black dots represent nanocrystal centroids measured from LC-STEM movies and the heat map is an interpolated surface

showing the local nucleation flux (nuclei/area/time) (see Supporting information for methods of generating nucleation flux maps). For relatively low supersaturation ratio (**Figure 2a**), few nuclei were observed initially, giving a low nucleation flux across the interface. As the reaction progressed, nucleation intensified in distinct interfacial domains with high nucleation flux, indicated by red and orange areas. Increased supersaturation ratio led to an overall larger number of nuclei being formed per unit area throughout the LC-STEM experiment with higher local nucleation fluxes occurring earlier in the time-lapsed data (**Figure 2b**). At higher magnification (**Figure 2c**), almost all nuclei formed with high flux before 30 s, after which nucleation greatly slowed down. There are two noteworthy aspects of the maps. First, the nucleation flux maps showed interfacial domains with locally high nucleation flux (*e.g.* **Figure 2b**, t = 41 s), as opposed to randomly distributed nucleation events on the surface. These interfacial domains of high local nucleation flux appeared in different and exclusive regions of the interface at different times during nucleation. Second, after the initial large nucleation flux at the highest supersaturation ratio, almost no nucleation events were observed after 30 seconds. Together, these two features strongly suggest that nucleation was heterogeneous and occurred at a limited number of nucleation sites.

To investigate the spatial variations in nucleation kinetics in more detail, static nucleation kinetic maps were generated by correlating nucleation induction time and nanoparticle spatial location. Briefly, these maps were generated by interpolating a 3D surface of the nucleation induction time given known values for each nanocrystal observed in the LC-STEM images (see Supporting information for methods). Each map derives from a single LC-STEM movie taken at a given experimental condition and shows a static representation of the local nucleation kinetics at the same spatial scale as the LC-STEM images. **Figure 3** shows nanometric spatial maps of nucleation kinetics for three different image magnifications and two different precursor

concentrations. The blue dots in each map represent positions of silver nanocrystals extracted from the last frame of the LC-STEM movie, while the heat map is the interpolated nucleation induction time. Yellow/white areas represent domains where nucleation happened late in the movie, *i.e.* slow nucleation, and black/red areas indicate where nucleation occurred early in the movie, *i.e.* fast nucleation. At the lowest relative supersaturation ratio (0.1 mM, 80 kx), the nucleation map was dominated by slow nucleation regions and interspersed with a few red/black 100 – 200 nm regions showing more rapid nucleation. As the supersaturation was increased by increasing LC-STEM magnification (0.1 mM, 100 kx), the nucleation map showed increased coverage of 100 – 200 nm red and black fast nucleation domains. We note that each domain contained at least 5 – 10 nanocrystals that nucleated within a few seconds of each other, indicating the appearance of domains was not an artifact of the map interpolation procedure. The nucleation map for the highest supersaturation ratio for 0.1 mM precursor (150 kx) showed rapid nucleation kinetics over much of the area with only a few single particles showing slow nucleation. We observed the same qualitative trend for the 0.2 mM precursor concentration when increasing supersaturation using the image magnification. For the same magnification, the 0.2 mM precursor concentration experiments showed higher coverage of fast nucleation domains compared to the 0.1 mM precursor concentration. The largest supersaturation ratio of all experiments (0.2 mM, 150 kx) showed uniformly rapid nucleation kinetics across the map.

Clearly, there was some preference for nanocrystals to nucleate in certain areas on the interface, but what caused the spatial variations in the nucleation kinetics of silver nanocrystals? Additionally, why does increasing supersaturation ratio nearly eliminate spatial variations in nucleation kinetics? Based on currently accepted classical and non-classical nucleation mechanisms, we consider three possible explanations for the observed spatial variations in

nucleation kinetics of silver nanocrystals. These include random variations in nucleation kinetics, spinodal decomposition, and heterogeneous nucleation. Nucleation is an inherently stochastic process, occurring randomly in time and space even for a constant supersaturation ratio and free energy barrier. It is possible this could lead to perceived spatial non-uniformities in nucleation kinetics. However, nucleation maps in **Figure 3** and **Figure S2** rule out this possibility by showing the significant impact of supersaturation on spatial non-uniformities in nucleation kinetics. Nucleation domains located at opposite sides of the map had similar nucleation times despite being separated by nearly a micron (**Figure 3b**), further indicating the domains were not due to random variations in nucleation but instead were physical in nature.

We have considered spinodal decomposition as a possible mechanism because prior LC-TEM experiments by Loh *et al.* showed evidence for this mechanism during metal nanocrystal nucleation in very thin liquid layers of ~50 nm.[26] Spinodal decomposition occurs when the supersaturation ratio is large enough to render the free energy barrier to nucleation insignificant.[52] Local solute concentration fluctuations cause spontaneous liquid-liquid phase separation to form precursor-rich and solvent-rich phases, followed by nucleation in the precursor rich phase. Two characteristic features of spinodal decomposition are the co-existence of small and large nanocrystals[52] and a diffusively controlled characteristic time scale for spinodal domain formation. Our LC-STEM images did not show a bimodal population of nanocrystal sizes (**Figure 1a-d**). The formation time of spinodal regions should scale as $\tau \approx \frac{l^2}{D}$, where D is the diffusion coefficient and l is the characteristic length scale.[26] Taking the characteristic feature size to be the size of the nucleation domains ($l \sim 100\, nm$) and the diffusion coefficient of silver atoms in liquid to be $D \sim 10^{-9}\, \frac{m^2}{s}$, we obtain a predicted time scale for spinodal domain formation to be $\tau \sim 10^{-5}\, s$, far shorter than the time scale of our experiments. While the patterns observed in our nucleation maps

are reminiscent of spinodal decomposition, inconsistences between our experiments and theory indicate spinodal decomposition is likely not the underlying mechanism.

An alternative hypothesis is that nanocrystals form with spatially varying nucleation kinetics due to heterogeneous nucleation. Interfacial defects, surface roughness, and surface functional groups decrease the local free energy barrier for nucleation by decreasing the nuclei-solvent interfacial energy or locally increasing supersaturation.[9] To test whether heterogeneous nucleation caused spatial variations in nucleation kinetics, we performed liquid phase atomic force microscopy (AFM) to investigate the properties of the solid/liquid interface. The AFM was operated in chemical force microscopy (CFM) imaging mode to show chemical contrast due to hydrophilic/hydrophobic interactions (see Supporting information for methods).[53, 54] The image in **Figure 4a** is an AFM height map of the interface and shows the interface was relatively flat with a surface roughness of about 3 nm. However, the phase contrast CFM image (**Figure 4b**) showed distinct domains with different hydrophilic and hydrophobic nature. Prior work established that attractive hydrophilic tip-surface interactions cause retarded phase shifts (dark contrast) in CFM images.[55] Moreover, the sizes of the low phase dark domains are on the same scale (~50 – 100 nm) as the domains of fast nucleation observed in the nucleation maps in **Figure 3**.

Silicon nitride surfaces possess silamine (Si-NH_2) and silanol (Si-OH) functional groups, each of which are hydrophilic and may act as heterogeneous nucleation sites.[6, 9, 10] Prior measurements have found the majority of groups on silicon nitride are silanol, with the fraction of silamine groups present ranging from 1% to 6%.[56, 57] We performed nanoparticle functional group labeling experiments to probe the spatial distribution of silanol and silamine groups to test our hypothesis that hydrophilic domains are composed of surface functional groups. The silicon nitride membranes were plasma treated in air and then silanized with (3-Aminopropyl)triethoxysilane

(APTES) to convert all silanol functional groups to amine groups, enabling their facile labeling with amide chemistry.[58] Amine surface groups created by silanization were labeled with 10 nm carboxylated gold nanoparticles by reacting 1-ethyl-3-(3-dimethylaminopropyl)carbodiimide hydrochloride (EDC) and N-hydroxysulfosuccinimide (sulfo-NHS) with the carboxyl groups, rendering the nanoparticles reactive to primary amines. Upon incubating the amine reactive nanoparticles with the silicon nitride surface, the nanoparticles covalently bind the amine groups and label the original positions of the silanol groups (see Supporting information for more details). This method also labels native silamine groups, but prior literature and control experiments indicated the silamine coverage was at least five times lower than the total functional group coverage (see Supporting information **Figure S5**). **Figures 4c-d** shows TEM images of gold nanoparticles conjugated to a plasma treated silicon nitride membrane surface, denoting the positions of silanol and silamine functional groups. The TEM images clearly show domains of functional groups on the surface with similar sizes as those in the CFM images (**Figure 4d**) and nucleation kinetic maps (**Figure 3**). The domains were not observed when the native silamine groups were specifically labeled (**Figure 4e**) or on the native silicon nitride surface without plasma treatment (**Figure S5a**). Silicon dioxide surfaces only possess silanol functional groups, so we performed similar labeling experiments on SiO_2 membranes to determine whether similar domains formed. We found that silanol groups also formed domains on SiO_2 after oxygen plasma treatment (**Figure S6**), suggesting silanol groups form domains on silicon nitride surfaces, as silicon nitride has similar surface chemistry to SiO_2 after exposure to air.[59] Air plasma generates O^{2-} and O^{-} gaseous species that react with the silicon nitride surface to generate additional Si-O groups and polymerize neighboring silanol groups *via* Si-O-Si siloxane bonds. The polymerized domains become hydrated in water and form domains of silanol groups.[60-65] Based on our labeling results

and prior literature, we conclude that oxygen plasma generation of silanol groups and their polymerization formed hydrophilic functional group domains on silicon nitride. Because our labeling method also marks silamine groups, it is possible that a minority fraction of silamine groups exist within the functional group domains.

Silanol and silamine functional groups are pronated or deprotonated depending on pH and have well-known pKa values.[66, 67] In our LC-STEM experiments, the electron beam modifies the pH by creating protons and gives a pH in the range of 5-6.[30] In this range, Si-OH is 50 – 100% deprotonated to the form $Si\text{-}O^-$, while $Si\text{-}NH_2$ is 100% protonated to $Si\text{-}NH_3^+$.(see calculations in Supporting information) Prior LC-TEM experiments showing pinning of positively charged gold nanorods during surface diffusion further support the existence of negatively charged, deprotonated silanol groups on the silicon nitride surface.[68, 69] Electrostatic attraction of hydrated Ag^+ ions to $Si\text{-}O^-$ groups could lead to a locally increased supersaturation ratio and nucleation rate on the functional group domains. Alternatively, a decreased interfacial energy penalty for heterogeneous nucleation on the functional group domains could similarly increase nucleation rate. It is currently unclear which phenomena enhances nucleation; however, the latter has a more significant impact on the nucleation rate in the context of CNT, which predicts the free energy barrier for nucleation decreases as the cube of interfacial energy.

Phenomenological nucleation model

CNT has been shown in multiple instances to quantitatively describe heterogeneous nucleation at solid-liquid interfaces,[11, 14, 35] so we have used CNT as the basis of a phenomenological model to support our experiments. We model the solid/liquid interface as two populations of nucleation sites, one with relatively low free energy barrier (functional group

domains) and the other population with a higher free energy barrier (surrounding areas). The free energy barrier distribution for each population is taken to be a normal distribution. Based on CNT, the expected heterogeneous nucleation rate for a given nucleation site (i) can be written as[70]

$$R_i = \nu exp\left[-\frac{\Delta G_{het,i}}{k_B T}\right] \quad (1)$$

$$\Delta G_{het,i} = \phi_i \Delta G_{hom}. \quad (2)$$

Here ν is the attempt frequency for nucleation, $\Delta G_{het,i}$ is the free energy barrier of nucleation site i, ΔG_{hom} is the free energy barrier for homogeneous nucleation, and ϕ_i is the free energy barrier reduction factor for nucleation site i, which depends on the contact angle of the nucleus and is confined to values between 0 – 1.[71] ΔG_{hom} is determined here using a model derived by Privman *et al.* for the nucleation of gold nanoparticles in aqueous solution.[72] Using experimental parameters relevant to our LC-STEM experiments, we estimate the homogeneous nucleation free energy barrier to be $\Delta G_{hom} = 25 - 40\ k_B T$ (see Supporting information methods for details). Two populations of nucleation sites are modeled with two normal distributions of free energy barrier reduction factors, $\phi_{i,1}$ and $\phi_{i,2}$, which are multiplied with ΔG_{hom} to determine the $\Delta G_{het,i}$ values for a given supersaturation ratio. The average nucleation rate is found by summing over all nucleation rates for a given population of nucleation sites:

$$\langle R \rangle = \nu \sum_{i=1}^{N} exp\left[-\frac{\Delta G_{het,i}}{k_B T}\right] \quad (3)$$

Figure 5 shows an example of two populations of nucleation sites used in this model, chosen such that the lowest free energy barrier sampled is ~10 $k_B T$, consistent with previously established values for heterogeneous nucleation.[6] We varied the homogeneous free energy barrier between $\Delta G_{hom} = 25 - 35\ k_B T$ ($S = 1.2x10^7 - 1.2x10^8$) and calculated the nucleation rate

for a given site as a function of the free energy barrier reduction factor, ϕ (**Figure 5b**). For the lowest supersaturation ratio (purple line), both populations of nucleation sites have slow nucleation kinetics, consistent with nearly uniform slow nucleation shown in the top left nucleation kinetic map in **Figure 3a**. In this case, all nucleation sites have high free energy barriers due to the large ΔG_{hom} and therefore slow nucleation rates. As supersaturation ratio is increased, nucleation of nearly all the low energy nucleation sites occurs with an appreciable rate and increasing portions of the high energy nucleation sites also have appreciable rates (*e.g.* red and blue curves, **Figure 5b**). This condition qualitatively corresponds to the nucleation map in **Figure 3b**. At the highest supersaturation, nucleation rates for the high and low energy nucleation sites are appreciable and have similar order of magnitude and therefore both nucleate relatively rapidly, consistent with the absence of spatial non-uniformities in the nucleation kinetic map for the highest supersaturation ratio (**Figure 3f**).

The average nucleation rate, <R>, was calculated for the low and high free energy barrier and all nucleation sites as a function of supersaturation ratio using equation (3), shown in **Figure 5c**. There is a nearly linear increase in total nucleation rate as a function of supersaturation ratio, consistent with the linear decrease in median nucleation induction time in **Figure 1g**. As expected from CNT, the slope for the low free energy barrier sites is larger than the high free energy sites. Interestingly, the model predicts that the high free energy barrier site nucleation rate only contributes significantly to the total nucleation rate at high supersaturation levels, which explains the trends in the number of particles vs. time data in **Figure 1e**. At low LC-STEM magnifications and supersaturation levels, the nucleation rate is dominated by the low free energy barrier nucleation sites and thus only one rate is observed after an initial lag time (*e.g.* 80 kx and 100 kx data). However, at high magnification and supersaturation ratio, there was an initially high

nucleation rate followed by a distinct decrease in slope after 20 seconds. In the context of our model, the change point in slope is due to depletion of low free energy barrier nucleation sites, leaving only high free energy sites with a lower nucleation rate.

Quantitative differences between the nucleation kinetic maps in **Figure 3** and nanoparticle labeling and CFM images in **Figure 4** are similarly explained by this model. There exists a hypothetical supersaturation ratio that enables nucleation to occur at an appreciable rate only on the functional group domains with essentially no nucleation elsewhere (*e.g.* **Figure 5b**, yellow line), which would lead to a nucleation map that appears identical to nanoparticle labeling images. However, the stochastic nature of nucleation dictates that even for a constant supersaturation and free energy barrier, nucleation will occur sporadically in time. This indicates that not all nuclei will form at the exact same time on the functional group domains, which will create random features in the nucleation maps that are not seen in the nanoparticle labeling experiments.

Conclusions

We investigated the heterogeneous nucleation of silver nanocrystals at a solid-liquid interface using LC-STEM. Nanoscale mapping of local nucleation kinetics demonstrated non-intuitive spatial variations in heterogeneous nucleation kinetics at a seemingly uniform interface. CFM imaging and functional group labeling experiments revealed that surface functional groups, specifically plasma generated silanol groups, were segregated into interfacial domains that acted as preferential nucleation sites. We derived a phenomenological nucleation model, which was qualitatively consistent with the spatial variations in nucleation kinetics and their dependence on supersaturation ratio**.** We expect these results will have implications in the broader chemistry community. First, our results illuminate that prior ensemble measurements of nucleation kinetics

on macroscopically homogeneous and uniform surfaces are an average of the nucleation kinetics at each nucleation site.[9, 11] In reality, microscopic spatial variations in surface chemistry on the macroscopically uniform surface lead to significant spatial variations in nucleation kinetics. As nucleation kinetics often determine crystal polymorph,[9] these microscopic variations must be considered when investigating morphology of crystals formed at solid-liquid interfaces. Secondly, our results represent a new microscopy and data analysis approach for measuring nanoscale variations in nucleation kinetics on a chemically heterogeneous surface. We expect a similar method could be applied to topologically heterogeneous surfaces as well. This approach could be applied to important materials systems where heterogeneous nucleation occurs at a chemically or topologically non-uniform interface, such as biomineralization, ice nucleation on aerosols, and polymorph selection in templated synthesis of complex oxide materials.

Supporting Information

Materials and methods; Computational methods for generating nucleation maps; Nucleation induction time maps at different imaging conditions; Functional group labeling control experiments; Functional group protonation calculations; CFM control experiments; Classical nucleation theory calculations.

Acknowledgements

T.J.W. acknowledges funding from Oak Ridge Associated Universities (ORAU, Award 17061851) and University of Maryland start-up funds. M.W. acknowledges funding from a Harry K. Wells Fellowship from the University of Maryland Energy Innovation Institute. C.P. acknowledges partial funding from Air Force Office of Scientific Research (Grant FA9550- 18-1-0144).

References

1. Bartels-Rausch, T., Ten things we need to know about ice and snow. *Nature* **2013,** *494*, 27.
2. Van Driessche, A. E. S.; Van Gerven, N.; Bomans, P. H. H.; Joosten, R. R. M.; Friedrich, H.; Gil-Carton, D.; Sommerdijk, N. A. J. M.; Sleutel, M., Molecular nucleation mechanisms and control strategies for crystal polymorph selection. *Nature* **2018,** *556*, 89.
3. Howes, P. D.; Chandrawati, R.; Stevens, M. M., Colloidal nanoparticles as advanced biological sensors. *Science* **2014,** *346* (6205), 1247390.
4. Dong, Z.; Feng, L.; Hao, Y.; Chen, M.; Gao, M.; Chao, Y.; Zhao, H.; Zhu, W.; Liu, J.; Liang, C.; Zhang, Q.; Liu, Z., Synthesis of Hollow Biomineralized CaCO3–Polydopamine Nanoparticles for Multimodal Imaging-Guided Cancer Photodynamic Therapy with Reduced Skin Photosensitivity. *J. Am. Chem. Soc*. **2018,** *140* (6), 2165-2178.
5. Smeets, P. J. M.; Cho, K. R.; Kempen, R. G. E.; Sommerdijk, N. A. J. M.; De Yoreo, J. J., Calcium carbonate nucleation driven by ion binding in a biomimetic matrix revealed by in situ electron microscopy. *Nat. Mater.***2015,** *14* (4), 394-399.
6. Chayen, N. E.; Saridakis, E.; Sear, R. P., Experiment and theory for heterogeneous nucleation of protein crystals in a porous medium. *Proc. Natl. Acad. Sci. U. S. A.* **2006,** *103* (3), 597-601.
7. Page, A. J.; Sear, R. P., Heterogeneous Nucleation in and out of Pores. *Phys. Rev. Lett.* **2006,** *97* (6), 065701.
8. Diao, Y.; Myerson, A. S.; Hatton, T. A.; Trout, B. L., Surface Design for Controlled Crystallization: The Role of Surface Chemistry and Nanoscale Pores in Heterogeneous Nucleation. *Langmuir* **2011,** *27* (9), 5324-5334.
9. Hu, Q.; Nielsen, M. H.; Freeman, C. L.; Hamm, L. M.; Tao, J.; Lee, J. R. I.; Han, T. Y. J.; Becker, U.; Harding, J. H.; Dove, P. M.; De Yoreo, J. J., The thermodynamics of calcite nucleation at organic interfaces: Classical vs. non-classical pathways. *Faraday Discuss.* **2012,** *159* (0), 509-523.
10. Aizenberg, J.; Black, A. J.; Whitesides, G. M., Control of crystal nucleation by patterned self-assembled monolayers. *Nature* **1999,** *398* (6727), 495-498.
11. Hamm, L. M.; Giuffre, A. J.; Han, N.; Tao, J.; Wang, D.; De Yoreo, J. J.; Dove, P. M., Reconciling disparate views of template-directed nucleation through measurement of calcite nucleation kinetics and binding energies. *Proc. Natl. Acad. Sci.* **2014,** *111* (4), 1304-1309.
12. Sear, R. P., Quantitative studies of crystal nucleation at constant supersaturation: experimental data and models. *CrystEngComm* **2014,** *16* (29), 6506-6522.
13. Yau, S. T.; Vekilov, P. G., Direct Observation of Nucleus Structure and Nucleation Pathways in Apoferritin Crystallization. *J. Am. Chem. Soc.* **2001,** *123* (6), 1080-1089.
14. Sleutel, M.; Lutsko, J.; Van Driessche, A. E. S.; Durán-Olivencia, M. A.; Maes, D., Observing classical nucleation theory at work by monitoring phase transitions with molecular precision. *Nat. Commun.* **2014,** *5*, 5598.
15. Chen, J.; Zhu, E.; Liu, J.; Zhang, S.; Lin, Z.; Duan, X.; Heinz, H.; Huang, Y.; De Yoreo, J. J., Building two-dimensional materials one row at a time: Avoiding the nucleation barrier. *Science* **2018,** *362* (6419), 1135-1139.
16. Ma, X.; Zhang, S.; Jiao, F.; Newcomb, C. J.; Zhang, Y.; Prakash, A.; Liao, Z.; Baer, M. D.; Mundy, C. J.; Pfaendtner, J.; Noy, A.; Chen, C.-L.; De Yoreo, J. J., Tuning crystallization pathways through sequence engineering of biomimetic polymers. *Nat. Mater.* **2017,** *16*, 767.
17. Liu, G.; Liu, J.; Sun, H.; Zheng, X.; Liu, Y.; Li, X.; Qi, H.; Bai, X.; Jackson, K. A.; Tao, X., In Situ Imaging of On-Surface, Solvent-Free Molecular Single-Crystal Growth. *J. Am. Chem. Soc.* **2015,** *137* (15), 4972-4975.

18. Lupulescu, A. I.; Rimer, J. D., In Situ Imaging of Silicalite-1 Surface Growth Reveals the Mechanism of Crystallization. *Science* **2014,** *344* (6185), 729-732.
19. Zheng, H.; Smith, R. K.; Jun, Y.-w.; Kisielowski, C.; Dahmen, U.; Alivisatos, A. P., Observation of Single Colloidal Platinum Nanocrystal Growth Trajectories. *Science* **2009,** *324* (5932), 1309-1312.
20. Woehl, T. J.; Park, C.; Evans, J. E.; Arslan, I.; Ristenpart, W. D.; Browning, N. D., Direct Observation of Aggregative Nanoparticle Growth: Kinetic Modeling of the Size Distribution and Growth Rate. *Nano Lett.* **2014,** *14* (1), 373-378.
21. Jungjohann, K. L.; Bliznakov, S.; Sutter, P. W.; Stach, E. A.; Sutter, E. A., In Situ Liquid Cell Electron Microscopy of the Solution Growth of Au–Pd Core–Shell Nanostructures. *Nano Lett.* **2013,** *13* (6), 2964-2970.
22. Yuk, J. M.; Park, J.; Ercius, P.; Kim, K.; Hellebusch, D. J.; Crommie, M. F.; Lee, J. Y.; Zettl, A.; Alivisatos, A. P., High-Resolution EM of Colloidal Nanocrystal Growth Using Graphene Liquid Cells. *Science* **2012,** *336* (6077), 61-64.
23. Hauwiller, M. R.; Ondry, J. C.; Chan, C. M.; Khandekar, P.; Yu, J.; Alivisatos, A. P., Gold Nanocrystal Etching as a Means of Probing the Dynamic Chemical Environment in Graphene Liquid Cell Electron Microscopy. *J. Am. Chem. Soc.* **2019,** *141* (10), 4428-4437.
24. Wu, J.; Gao, W.; Yang, H.; Zuo, J.-M., Dissolution Kinetics of Oxidative Etching of Cubic and Icosahedral Platinum Nanoparticles Revealed by in Situ Liquid Transmission Electron Microscopy. *ACS Nano* **2017,** *11* (2), 1696-1703.
25. Hauwiller, M. R.; Frechette, L. B.; Jones, M. R.; Ondry, J. C.; Rotskoff, G. M.; Geissler, P.; Alivisatos, A. P., Unraveling Kinetically-Driven Mechanisms of Gold Nanocrystal Shape Transformations Using Graphene Liquid Cell Electron Microscopy. *Nano Lett.* **2018,** *18* (9), 5731-5737.
26. Loh, N. D.; Sen, S.; Bosman, M.; Tan, S. F.; Zhong, J.; Nijhuis, C. A.; Král, P.; Matsudaira, P.; Mirsaidov, U., Multistep nucleation of nanocrystals in aqueous solution. *Nat. Chem.* **2016,** *9*, 77.
27. Wang, M.; Park, C.; Woehl, T. J., Quantifying the Nucleation and Growth Kinetics of Electron Beam Nanochemistry with Liquid Cell Scanning Transmission Electron Microscopy. *Chem. Mater.* **2018,** *30* (21), 7727-7736.
28. Woehl, T. J.; Evans, J. E.; Arslan, I.; Ristenpart, W. D.; Browning, N. D., Direct in Situ Determination of the Mechanisms Controlling Nanoparticle Nucleation and Growth. *ACS Nano* **2012,** *6* (10), 8599-8610.
29. WOEHL, T. J.; ABELLAN, P., Defining the radiation chemistry during liquid cell electron microscopy to enable visualization of nanomaterial growth and degradation dynamics. *J. Microsc.* **2017,** *265* (2), 135-147.
30. Schneider, N. M.; Norton, M. M.; Mendel, B. J.; Grogan, J. M.; Ross, F. M.; Bau, H. H., Electron–Water Interactions and Implications for Liquid Cell Electron Microscopy. *J. Phys. Chem. C* **2014,** *118* (38), 22373-22382.
31. Park, J. H.; Schneider, N. M.; Grogan, J. M.; Reuter, M. C.; Bau, H. H.; Kodambaka, S.; Ross, F. M., Control of Electron Beam-Induced Au Nanocrystal Growth Kinetics through Solution Chemistry. *Nano Lett.* **2015,** *15* (8), 5314-5320.
32. Grogan, J. M.; Schneider, N. M.; Ross, F. M.; Bau, H. H., Bubble and Pattern Formation in Liquid Induced by an Electron Beam. *Nano Lett.* **2014,** *14* (1), 359-364.
33. Moser, T. H.; Mehta, H.; Park, C.; Kelly, R. T.; Shokuhfar, T.; Evans, J. E., The role of electron irradiation history in liquid cell transmission electron microscopy. *Sci. Adv.* **2018,** *4* (4), eaaq1202.
34. Jun, Y.-S.; Kim, D.; Neil, C. W., Heterogeneous Nucleation and Growth of Nanoparticles at Environmental Interfaces. *Acc. Chem. Res.* **2016,** *49* (9), 1681-1690.
35. Li, Q.; Jun, Y.-S., The apparent activation energy and pre-exponential kinetic factor for heterogeneous calcium carbonate nucleation on quartz. *Commun. Chem.* **2018,** *1* (1), 56.

36. Smeets, P. J. M.; Finney, A. R.; Habraken, W. J. E. M.; Nudelman, F.; Friedrich, H.; Laven, J.; De Yoreo, J. J.; Rodger, P. M.; Sommerdijk, N. A. J. M., A classical view on nonclassical nucleation. *Proc. Natl. Acad. Sci.* **2017,** *114* (38), E7882-E7890.
37. De Yoreo, J. J.; Vekilov, P. G., Principles of crystal nucleation and growth. *Rev. Mineral. Geochem.* **2003,** *54*, 57-93.
38. Zhang, X.; Zhang, F.; Wang, Y.; Schulman, D. S.; Zhang, T.; Bansal, A.; Alem, N.; Das, S.; Crespi, V. H.; Terrones, M.; Redwing, J. M., Defect-Controlled Nucleation and Orientation of WSe2 on hBN: A Route to Single-Crystal Epitaxial Monolayers. *ACS Nano* **2019,** *13* (3), 3341-3352.
39. Fenton, J. L.; Steimle, B. C.; Schaak, R. E., Tunable intraparticle frameworks for creating complex heterostructured nanoparticle libraries. *Science* **2018,** *360* (6388), 513-517.
40. Ding, K.; Cullen, D. A.; Zhang, L.; Cao, Z.; Roy, A. D.; Ivanov, I. N.; Cao, D., A general synthesis approach for supported bimetallic nanoparticles via surface inorganometallic chemistry. *Science* **2018,** *362* (6414), 560-564.
41. Wong, A.; Liu, Q.; Griffin, S.; Nicholls, A.; Regalbuto, J. R., Synthesis of ultrasmall, homogeneously alloyed, bimetallic nanoparticles on silica supports. *Science* **2017**, eaao6538.
42. Fu, Y.; Zheng, W.; Wang, X.; Hautzinger, M. P.; Pan, D.; Dang, L.; Wright, J. C.; Pan, A.; Jin, S., Multicolor Heterostructures of Two-Dimensional Layered Halide Perovskites that Show Interlayer Energy Transfer. *J. Am. Chem. Soc.* **2018,** *140* (46), 15675-15683.
43. Van Vleet, M. J.; Weng, T.; Li, X.; Schmidt, J. R., In Situ, Time-Resolved, and Mechanistic Studies of Metal–Organic Framework Nucleation and Growth. *Chem. Rev.* **2018,** *118* (7), 3681-3721.
44. Wang, X.-G.; Cheng, Q.; Yu, Y.; Zhang, X.-Z., Controlled Nucleation and Controlled Growth for Size Predicable Synthesis of Nanoscale Metal–Organic Frameworks (MOFs): A General and Scalable Approach. *Angew. Chem., Int. Ed.* **2018,** *57* (26), 7836-7840.
45. Lan, X.; Huang, N.; Wang, J.; Wang, T., A general and facile strategy for precisely controlling the crystal size of monodispersed metal–organic frameworks via separating the nucleation and growth. *Chem. Commun.* **2018,** *54* (6), 584-587.
46. Udayabhaskararao, T.; Kazes, M.; Houben, L.; Lin, H.; Oron, D., Nucleation, Growth, and Structural Transformations of Perovskite Nanocrystals. *Chem. Mater.* **2017,** *29* (3), 1302-1308.
47. Yao, Z.; Jones, T. W.; Grigore, M.; Duffy, N. W.; Anderson, K. F.; Dunbar, R. B.; Feron, K.; Hao, F.; Lin, H.; Wilson, G. J., Tunable Crystallization and Nucleation of Planar CH3NH3PbI3 through Solvent-Modified Interdiffusion. *ACS Appl. Mater. Interfaces* **2018,** *10* (17), 14673-14683.
48. Cao, X.; Zhi, L.; Jia, Y.; Li, Y.; Zhao, K.; Cui, X.; Ci, L.; Zhuang, D.; Wei, J., A Review of the Role of Solvents in Formation of High-Quality Solution-Processed Perovskite Films. *ACS Appl. Mater. Interfaces* **2019,** *11* (8), 7639-7654.
49. Lee, J. W.; Yu, H.; Lee, K.; Bae, S.; Kim, J.; Han, G. R.; Hwang, D.; Kim, S. K.; Jang, J., Highly Crystalline Perovskite-Based Photovoltaics via Two-Dimensional Liquid Cage Annealing Strategy. *J. Am. Chem. Soc.* **2019,** *141* (14), 5808-5814.
50. Wang, Y.; Li, L.; Liang, H.; Xing, Y.; Yan, L.; Dai, P.; Gu, X.; Zhao, G.; Zhao, X., Superstructure of a Metal–Organic Framework Derived from Microdroplet Flow Reaction: An Intermediate State of Crystallization by Particle Attachment. *ACS Nano* **2019,** *13* (3), 2901-2912.
51. van Embden, J.; Sader, J. E.; Davidson, M.; Mulvaney, P., Evolution of Colloidal Nanocrystals: Theory and Modeling of their Nucleation and Growth. *J. Phys. Chem. C* **2009,** *113* (37), 16342-16355.
52. Wallace, A. F.; Hedges, L. O.; Fernandez-Martinez, A.; Raiteri, P.; Gale, J. D.; Waychunas, G. A.; Whitelam, S.; Banfield, J. F.; De Yoreo, J. J., Microscopic Evidence for Liquid-Liquid Separation in Supersaturated CaCO₃ Solutions. *Science* **2013,** *341* (6148), 885-889.
53. Noy, A.; Sanders, C. H.; Vezenov, D. V.; Wong, S. S.; Lieber, C. M., Chemically-Sensitive Imaging in Tapping Mode by Chemical Force Microscopy: Relationship between Phase Lag and Adhesion. *Langmuir* **1998,** *14* (7), 1508-1511.

54. Ashby, P. D.; Lieber, C. M., Ultra-Sensitive Imaging and Interfacial Analysis of Patterned Hydrophilic SAM Surfaces Using Energy Dissipation Chemical Force Microscopy. *J. Am. Chem. Soc.* **2005,** *127* (18), 6814-6818.
55. Finot, M. O.; McDermott, M. T., High-Resolution Chemical Mapping of Surface Bound Functional Groups with Tapping-Mode Scanning Force Microscopy. *J. Am. Chem. Soc.* **1997,** *119* (36), 8564-8565.
56. Bousse, L.; Mostarshed, S., The zeta potential of silicon nitride thin films. *J. Electroanal. Chem.* **1991,** *302* (1), 269-274.
57. Guan, W.; Rajan, N. K.; Duan, X.; Reed, M. A., Quantitative probing of surface charges at dielectric–electrolyte interfaces. *Lab Chip* **2013,** *13* (7), 1431-1436.
58. Robertson, A. W.; Zhu, G.; Mehdi, B. L.; Jacobs, R. M. J.; De Yoreo, J.; Browning, N. D., Nanoparticle Immobilization for Controllable Experiments in Liquid-Cell Transmission Electron Microscopy. *ACS Appl. Mater. Interfaces* **2018,** *10* (26), 22801-22808.
59. Kennedy, G. P.; Buiu, O.; Taylor, S., Oxidation of silicon nitride films in an oxygen plasma. *J. Appl. Phys* **1999,** *85* (6), 3319-3326.
60. Zhuravlev, L. T.; Potapov, V. V., Density of silanol groups on the surface of silica precipitated from a hydrothermal solution. *Russ. J. Phys. Chem.* **2006,** *80* (7), 1119-1128.
61. Zhuravlev, L. T., The surface chemistry of amorphous silica. Zhuravlev model. *Colloids Surf., A* **2000,** *173* (1), 1-38.
62. Jiang, L.; Li, S.; Wang, J.; Yang, L.; Sun, Q.; Li, Z., Surface Wettability of Oxygen Plasma Treated Porous Silicon. *J. Nanomater.* **2014,** *2014*, 6.
63. Suni, T.; Henttinen, K.; Suni, I.; Mäkinen, J., Effects of Plasma Activation on Hydrophilic Bonding of Si and SiO2. *J. Electrochem. Soc.* **2002,** *149* (6), G348-G351.
64. Kaya, S.; Rajan, P.; Dasari, H.; Ingram, D. C.; Jadwisienczak, W.; Rahman, F., A Systematic Study of Plasma Activation of Silicon Surfaces for Self Assembly. *ACS Appl. Mater. Interfaces* **2015,** *7* (45), 25024-25031.
65. Sneh, O.; George, S. M., Thermal Stability of Hydroxyl Groups on a Well-Defined Silica Surface. *J. Phys. Chem.* **1995,** *99* (13), 4639-4647.
66. Cloarec, J.-P.; Chevalier, C.; Genest, J.; Beauvais, J.; Chamas, H.; Chevolot, Y.; Baron, T.; Souifi, A., pH driven addressing of silicon nanowires onto Si3N4/SiO2micro-patterned surfaces. *Nanotechnology* **2016,** *27* (29), 295602.
67. Tsukruk, V. V.; Bliznyuk, V. N., Adhesive and Friction Forces between Chemically Modified Silicon and Silicon Nitride Surfaces. *Langmuir* **1998,** *14* (2), 446-455.
68. Chee, S. W.; Anand, U.; Bisht, G.; Tan, S. F.; Mirsaidov, U., Direct Observations of the Rotation and Translation of Anisotropic Nanoparticles Adsorbed at a Liquid–Solid Interface. *Nano Lett.* **2019,** *19* (5), 2871-2878.
69. Chee, S. W.; Baraissov, Z.; Loh, N. D.; Matsudaira, P. T.; Mirsaidov, U., Desorption-Mediated Motion of Nanoparticles at the Liquid–Solid Interface. *J. Phys. Chem. C* **2016,** *120* (36), 20462-20470.
70. Sear, R. P.; Howard, M., Modeling dual pathways for the metazoan spindle assembly checkpoint. *Proc. Natl. Acad. Sci.* **2006,** *103* (45), 16758-16763.
71. Thanh, N. T. K.; Maclean, N.; Mahiddine, S., Mechanisms of Nucleation and Growth of Nanoparticles in Solution. *Chem. Rev.* **2014,** *114* (15), 7610-7630.
72. Robb, D. T.; Privman, V., Model of Nanocrystal Formation in Solution by Burst Nucleation and Diffusional Growth. *Langmuir* **2008,** *24* (1), 26-35.

Figures

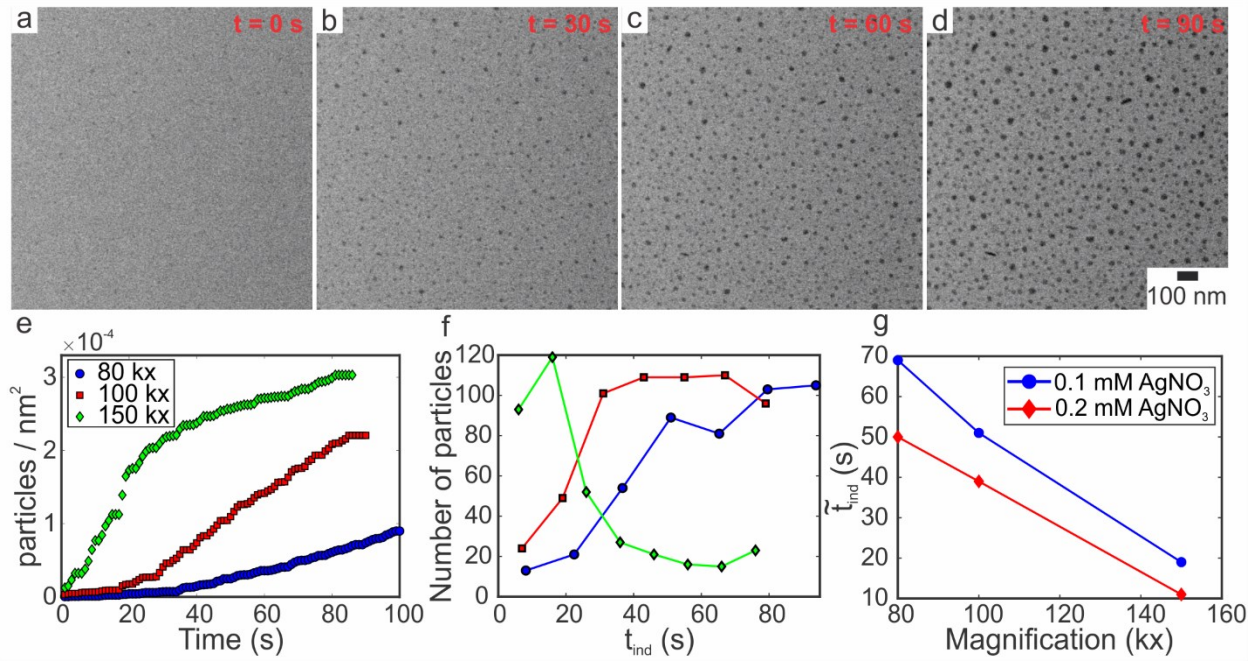

Figure 1. (a-d) Time lapsed bright field STEM images of silver nucleation for an image magnification of 100 kx and precursor concentration of 0.1 mM $AgNO_3$ (beam current (i_e) of i_e= 31 pA, dose rate ($\dot{d}$) of $\dot{d}$ = 1.3 MGy/s) e) Number of particles per area as a function of time and magnification. f) Distribution of nucleation induction times as a function of magnification, and g) Median nucleation induction time as a function of magnification and precursor concentration.

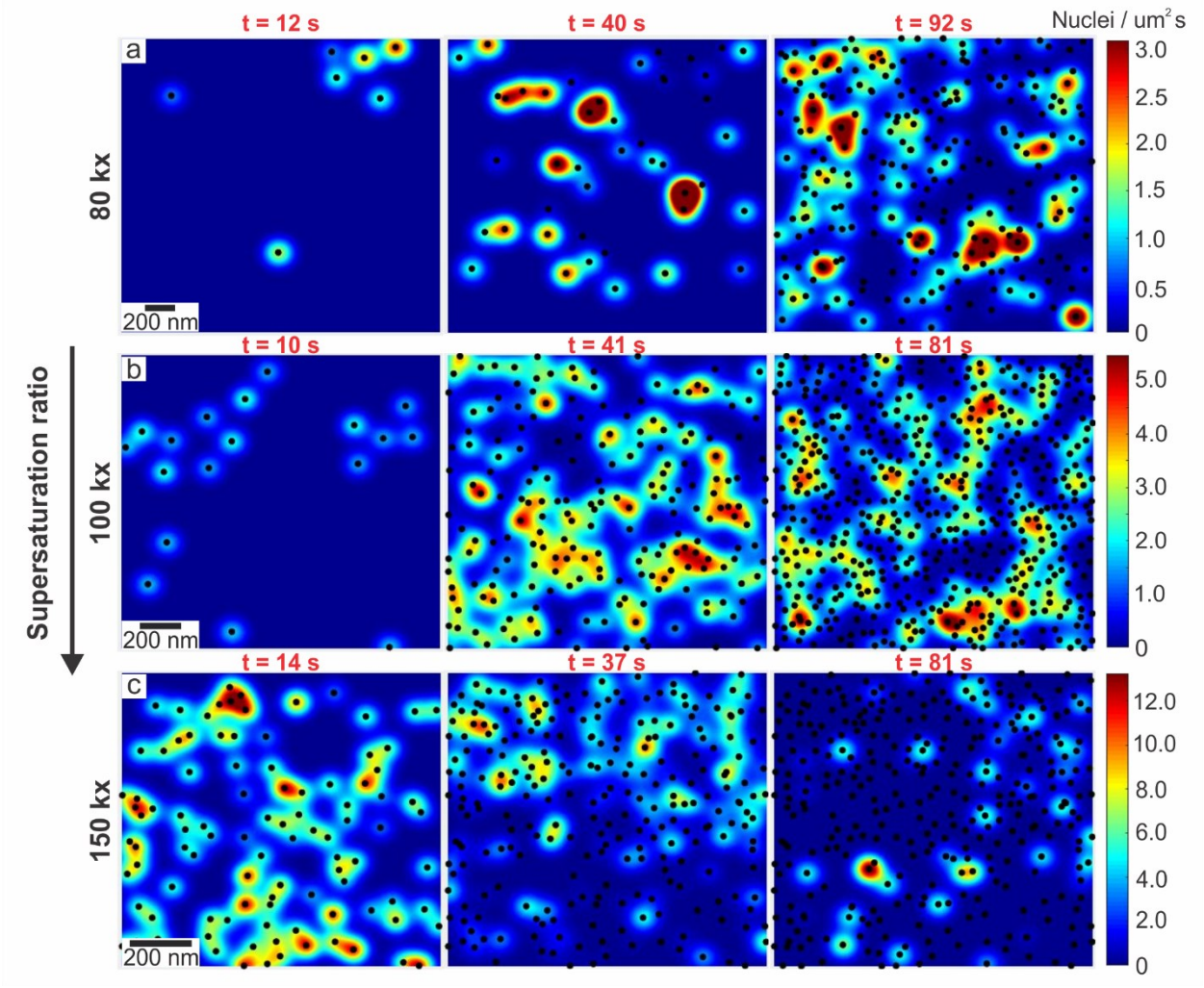

Figure 2. Time-lapsed nucleation flux maps for a precursor concentration of 0.1 mM $AgNO_3$ and LC-STEM magnifications of a) 80 kx (i_e= 31 pA, $\dot{d}$ = 0.7 MGy/s), b) 100 kx (i_e= 31 pA, $\dot{d}$ = 1.3 MGy/s), and c) 150 kx (i_e= 31 pA, $\dot{d}$ = 3.0 MGy/s). The black dots are centroids of silver nanocrystals formed during each LC-STEM experiment, while the color map corresponds to the interpolated nuclei flux. Red and orange areas correspond to high flux (higher nucleation rate), and blue and teal areas represent low flux (lower nucleation rate).

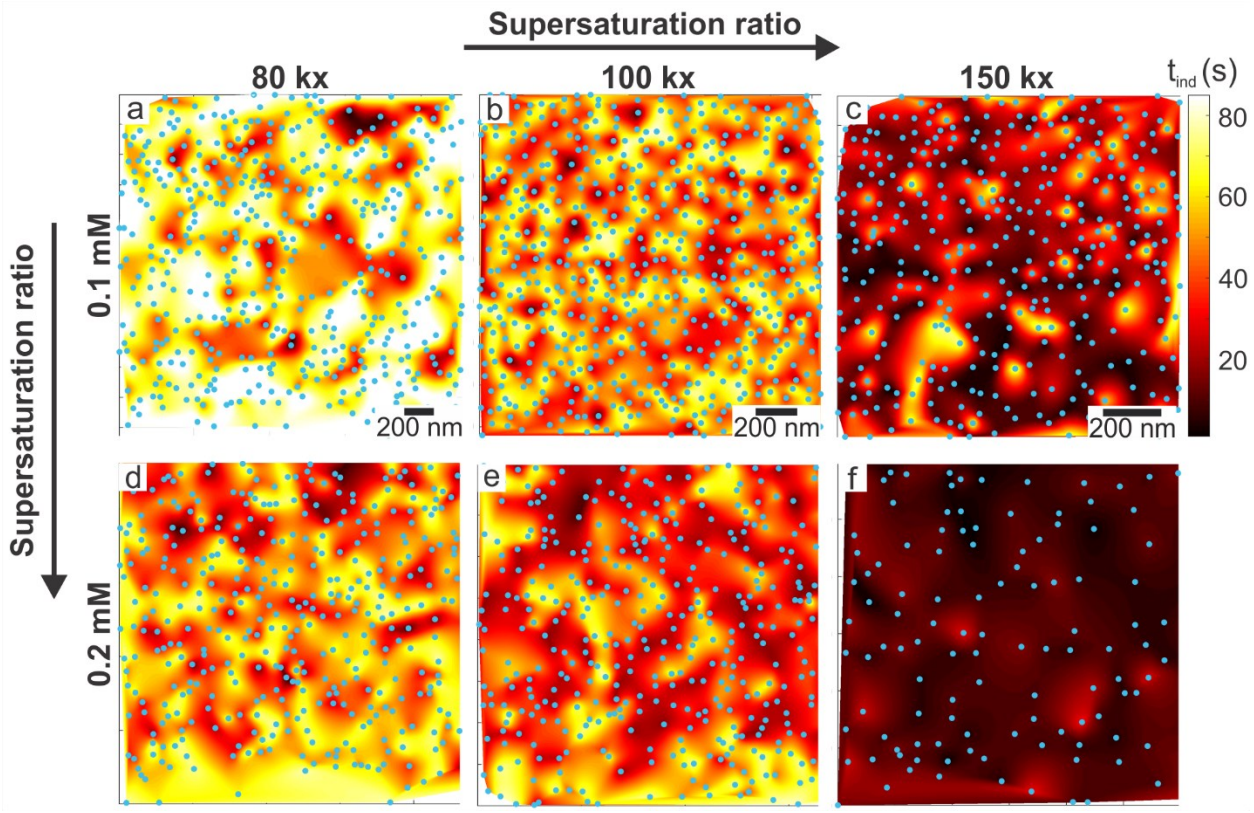

Figure 3. Static nanometric spatial maps of silver nucleation induction times as a function of LC-STEM magnification and precursor concentration. The beam current for all experiments was 31 pA. Top row: 0.1 mM $AgNO_3$ at magnifications of a) 80 kx ($\dot{d}$ = 0.7 MGy/s), b) 100 kx ($\dot{d}$ = 1.3 MGy/s), and c) 150 kx ($\dot{d}$ = 3.0 MGy/s). Bottom row: 0.2 mM $AgNO_3$ at magnifications of d) 80 kx, e) 100 kx, and f) 150 kx. The blue dots are centroids of all silver nanocrystals formed during each LC-STEM experiment, while the color map corresponds to the interpolated local nucleation induction time. Yellow and white areas correspond to large nucleation induction times (low nucleation rate) while red and black are small nucleation induction times (high nucleation rate).

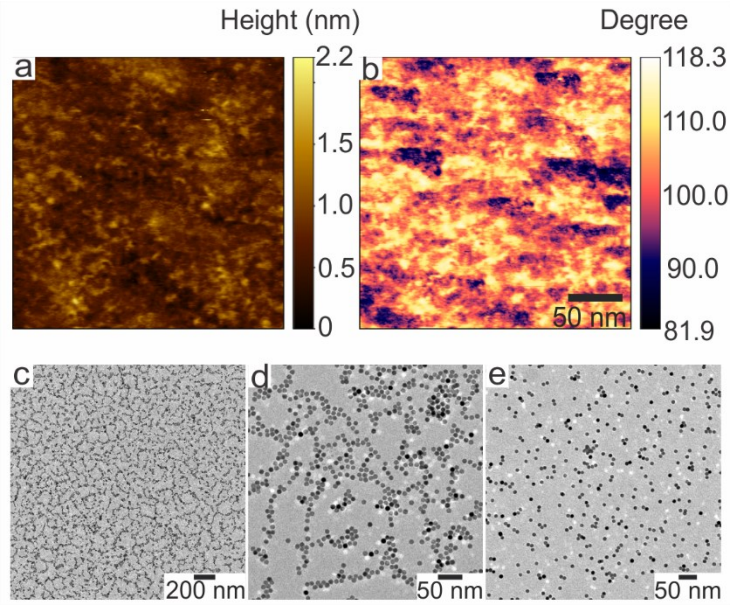

Figure 4. a)-b) Liquid phase AFM and CFM of a plasma treated silicon nitride membrane. a) Tapping mode AFM height image, b) tapping mode CFM phase image. c)-d) Low and high magnification TEM images of gold nanoparticle labeled functional groups (silanol and silamine) on a plasma treated silicon nitride membrane. e) TEM image of gold nanoparticles labeling only the native silamine groups on a plasma treated silicon nitride membrane.

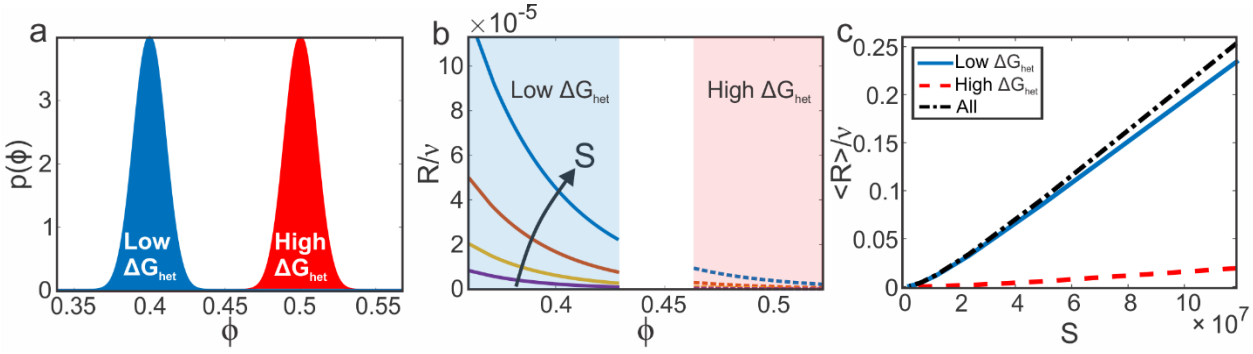

Figure 5. Phenomenological nucleation model. (a) Two populations of nucleation sites with low and high free energy barrier are modeled by two normally distributed probability distribution functions (PDFs) for nucleation site free energy barrier reduction factor, $p(\phi)$. (b) Normalized nucleation rate as a function of free energy barrier reduction factor and supersaturation ratio, calculated from equation (2). Solid lines were calculated by sampling values from the low ΔG_{het} PDF (blue PDF in (a)), while dashed lines were sampled from the high ΔG_{het} PDF (red PDF in (a)). (c) Average normalized nucleation rates calculated from equation (3) for low and high ΔG_{het} nucleation sites and all nucleation sites, as a function of supersaturation ratio.

TOC Figure

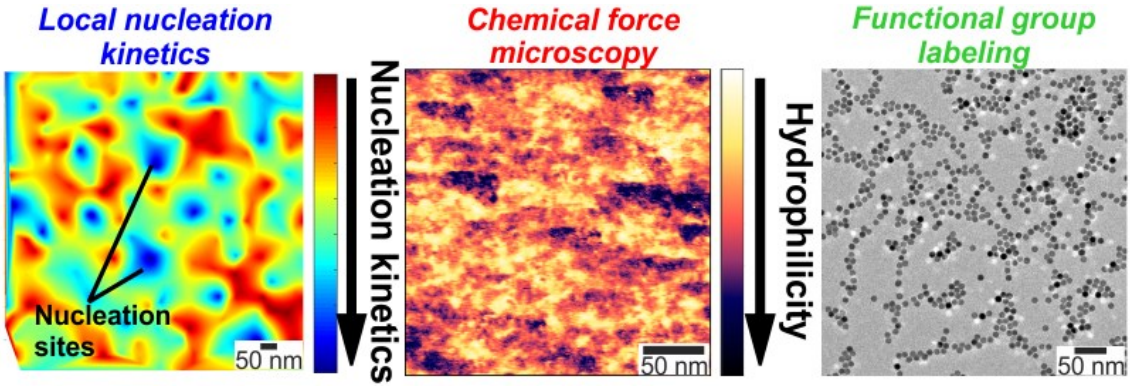
Local nucleation kinetics
Chemical force microscopy
Functional group labeling
Nucleation sites
50 nm
Nucleation kinetics
50 nm
Hydrophilicity
50 nm